Cake Structure in Dead-End Membrane Filtration: Monte Carlo Simulations

Albert S. Kim[1]* and Eric M.V. Hoek[2]

[1]*Department of Civil and Environmental Engineering*
University of Hawaii at Manoa
Honolulu, HI 96822
[2]*Department of Chemical and Environmental Engineering*
University of California
Riverside, CA 92521

ABSTRACT

A statistical mechanical approach for predicting the long-term gradual flux decline due to colloid-cake formation in dead-end membrane filtration is presented. Monte Carlo simulations of cake layers composed of interacting colloidal particles are performed to predict volume fractions and corresponding radial distribution functions. The total osmotic pressure in the cake layer is extracted from interparticle interactions and the radial distribution function. The extracted osmotic pressure predictions are in good agreement with applied pressure, verifying the accuracy of the simulation method. The simulation method is then used to investigate the effect of particle size, ionic strength, zeta potential, and applied pressure on the cake structure, which is represented by the volume fraction and the radial distribution function. Finally, the influence of these effects on permeate flux decline during the dead-end membrane filtration of interacting colloidal particles is predicted and qualitatively compared to previously published experimental data.

Key words: membrane filtration; membrane fouling; cake structure; cake volume fraction; NPT Monte Carlo simulation

INTRODUCTION

MICROFILTRATION (MF) AND ULTRAFILTRATION (UF) are pressure-driven membrane separation processes capable of removing suspended and colloidal matter from a solvent such as water. MF and UF are widely used to remove colloidal particles and micro-organisms in drinking water treatment, as well as to treat secondary or tertiary effluent in wastewater treatment (Wiesner *et al.*, 1994; Zeman and Zydney, 1996; Reith and Birken-

head, 1998). However, filtration performance is often limited due to the buildup of retained solutes at the membrane surface. This buildup may be classified into two categories: (1) concentration polarization (CP), and (2) formation of a "cake" between CP layer and the membrane surface.

Many models have been used to investigate the influence of concentration polarization on permeate flux decline (Kedem and Katchalsky, 1958; Vilker *et al.*, 1981; Reihanian *et al.*, 1983; Van Den Berg and Smolders,

*Corresponding author: Department of Civil Engineering, University of Hawaii at Manoa, Honolulu, HI 96822. *Phone*: 808-956-3718; *Fax*: 808-956-5014; *E-mail*: AlbertSK@hawaii.edu

1990; Bhattacharjee *et al.*, 1994, 1999; Elimelech and Bhattacharjee, 1998). However, in most practical applications, the effect of concentration polarization on permeate flux is rarely measurable because the transition from CP to cake formation occurs almost immediately (Song and Elimelech, 1995). In most crossflow membrane filtration theories, the CP layer resistance is assumed negligible in the presence of a cake, and thus the focus of flux decline models is on the transient cake resistance (Romero and Davis, 1988, 1990; Song and Elimelech, 1995; Bacchin *et al.*, 2002). Moreover, the cake resistance may be estimated by assuming a uniform porous structure (Carman, 1939) or a sphere-in-cell model (Happel, 1958; Happel and Brenner, 1991) with an arbitrary maximum packing ratio (Song and Elimelech, 1995; Faibish *et al.*, 1998).

Postulation of a solid-like fixed structure of hard spheres neglects the importance of particle–particle interactions between charged colloidal particles, and reveals little about the true structure of a cake layer. Most recent studies that have focused on the influence of particle–particle interactions (Petsev *et al.*, 1993; Bowen and Jenner, 1995; Holt *et al.*, 1995; Jönsson and Jönsson, 1996) were based on cell models. Most studies used a hexagonal close-packed structure, which was fixed for both the concentration polarization and the cake layer while computing interactions. Such *a priori* assumption of the solution structure is inadequate to describe the liquid-like disordered structure of a concentration polarization layer (Batchelor, 1972), and it is also questionable whether the cake structure follows such a crystalline pattern. Furthermore, none of the models are capable of predicting the permeate flux decline from a *realistic* cake structure for physically and chemically interacting colloidal particles.

Dead-end membrane filtration is not of practical interest for most filtration applications due to the rapid flux decline that results, but it is effectively used for specific separations such as pilot-scale tests (Decarolis *et al.*, 2001) or full-scale operation when coupled with a back-pulsing technique (Willemse and Brekvoort, 1999). Absence of an axial shear rate clearly distinguishes the dead-end filtration from the crossflow filtration during the cake build-up on the membrane surface. The structural variance of the cake layer due to tangential shear has not been extensively studied, but future research efforts may include crossflow effects by using a dynamic simulation method. Therefore, it is still valuable to investigate cake structures determined by interparticle colloidal interactions and applied pressure in the absence of crossflow.

In this paper, a fundamental statistical mechanics approach is used to determine the quasi-equilibrium structure of cake layers accounting for interparticle interactions and operating conditions. Isothermal-isobaric

Monte Carlo simulations are performed for a system of spherical particles interacting through a Derjaguin-Landau-Verwey-Overweek (DLVO) potential (Derjaguin and Landau, 1941; Verwey and Overbeek, 1948) to obtain the radial distribution function of the particulate system. Cake layer growth and flux decline are estimated by incorporating the pressure-dependent cake properties into the convection–diffusion equation and coupling those results with the dead-end cake filtration model. Finally, the results predicted from the model calculations are qualitatively compared to previously published experimental dead-end filtration data.

THEORETICAL BACKGROUND

The physical situation being considered is illustrated in Fig. 1. Interacting, rigid spherical particles with a volume fraction ϕ_b are carried from the bulk to the membrane surface by the permeate flux, v_w, initially establishing a concentration polarization layer. The cake layer is characterized by vanishing gradient of volume fraction (or porosity) with respect to y, and forms between the membrane surface and the concentration polarization layer. In the presence of a cake layer, CP layer resistance is assumed negligible, and transient flux decline results from the increasing thickness of the cake layer.

Mathematical model for dead-end membrane filtration

The governing dead-end cake filtration model originates from a transient mass balance on a growing cake layer, and is typically written as

$$\frac{\partial \phi}{\partial t} = \frac{\partial}{\partial y}\left(D\frac{\partial \phi}{\partial y} - v\phi\right), \tag{1}$$

where ν is the solvent velocity, D is the particle diffusion coefficient, and ϕ is the particle volume fraction. Integration of Equation (1) from the membrane surface to the top of the concentration polarization layer, as shown in Fig. 1, yields (Romero and Davis, 1990)
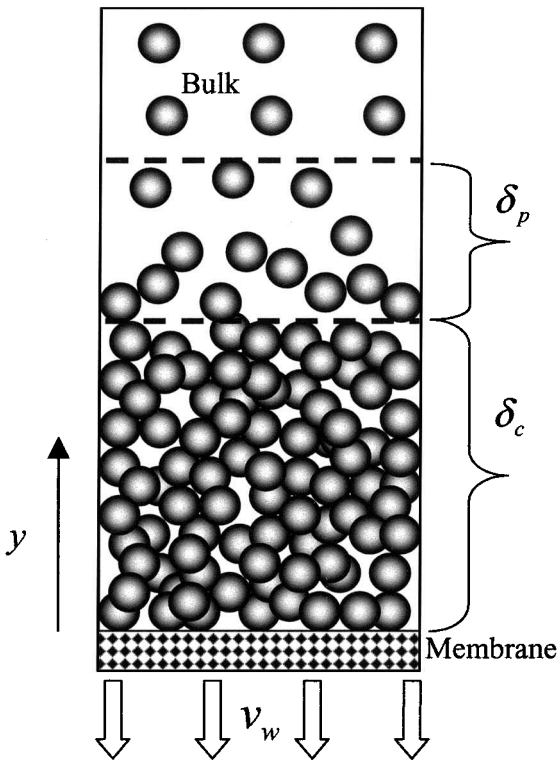
$$\frac{\partial}{\partial t}\left[\int_{\delta_c}^{\delta_c+\delta_p}(\phi-\phi_b)\,dy + (\phi_c-\phi_b)\delta_c\right] = v_w\phi_b, \tag{2}$$

where δ_p and δ_c are the thickness of CP layer and the cake layer, respectively, ϕ_c is the particle volume fraction of the cake layer, and $v_w(=-v)$ is the permeate velocity. Rewriting the left-hand side of Equation (2) yields

$$\phi_c\frac{\partial \delta_c}{\partial t} + \frac{\partial}{\partial t}\left[\int_{\delta_c}^{\delta_c+\delta_p}\phi\,dy\right] - \phi_b\frac{\partial \delta_t}{\partial t} = v_w\phi_b, \tag{3}$$

where

$$\delta_t = \delta_c + \delta_p. \tag{4}$$

Figure 1. Schematic diagram of the concentration polarization and the cake layer in the dead-end membrane filtration. In this diagram δ_p and δ_c represent the thickness of the concentration polarization and the cake layer, respectively.

The first term in Equation (3) represents the growth rate of a cake layer of volume fraction, ϕ_c, the second term corresponds the accumulation of particles in the CP layer, and the third term reflects the increase in total boundary layer thickness, δ_t, defined by Equation (4). Particles with volume fraction of ϕ_b in suspension are introduced to the CP layer with a velocity v_w, and contribute mass influx at $y = \delta_t$. At the same time, the thickness δ_t increases because when the particle volume fraction reaches a maximum volume fraction, ϕ_c, for a given set of physical and chemical conditions, it is considered part of the cake layer. Therefore, the third term of Equation (3) effectively quantifies the particle mass flux $v_w\phi_b$ out of the concentration polarization layer and into the cake layer at $y = \delta_c$.

The total pressure drop ΔP across the membrane, the concentration polarization layer, and the cake layer is therefore described by

$$\Delta P = \Delta P_m + \Delta P_p + \Delta P_c, \tag{5}$$

where, ΔP_m, ΔP_p, and ΔP_c are the pressure drops across the membrane, the concentration polarization layer, and the cake layer, respectively (Song and Elimelech, 1995). They are

$$\Delta P_m = \mu R_m v_w \tag{6}$$

$$\Delta P_p = \int_{\delta_c}^{\delta_c + \delta_p} nF dy \tag{7}$$

$$\Delta P_c = \mu r_c \delta_c v_w \tag{8}$$

where, n is the number concentration of particles, F is the hydrodynamic drag force acting on each particle in the concentration polarization layer, μ is the solvent viscosity, and R_m is the membrane hydraulic resistance. The specific cake resistance, r_c, is related to the cake volume fraction, ϕ_c, via the Kozeny-Carman equation (Carman, 1939)

$$r_c = \frac{45\phi_c^2}{a^2(1 - \phi_c)^3}, \tag{9}$$

where a is the particle radius of a monodisperse colloidal suspension. Equation (7) was obtained by considering that the pressure gradient is balanced with the interparticle force density. Once a cake layer forms, the resistance of the CP layer becomes negligible because the volume fraction and thickness are small compared to the cake layer. Flux at constant pressure is solely governed by the increasing cake layer thickness of constant cake volume fraction, determined from Equation (8). The functional form of Equation (9) (i.e., dependency on the cake volume fraction, ϕ_c) does not assume any specific cake structure, and the pre-factor, 45, is based on the specific surface of a spherical particle and an experimentally determined constant (Elimelech *et al.*, 1995). Although the Kozeny-Carman equation has been derived to account for the hydrodynamic resistance of a packed bed, we presume Equation (9) is available for the cake structure of certain volume fraction without significant errors. Therefore, the integral mass balance Equation (3) and the permeate flux Equation (5) are simplified and may be rewritten as

$$(\phi_c - \phi_b)\frac{d\delta_c}{dt} = v_w\phi_b \tag{10}$$

and

$$v_w = \frac{\Delta P}{\mu(R_m + r_c\delta_c)}, \tag{11}$$

respectively. Substitution of Equation (11) into (10) and integrating across the cake layer yields

$$v_w = \frac{v_{w0}}{\sqrt{1 + \alpha t}}, \tag{12}$$

where

$$v_{w0} = \frac{\Delta P}{\mu R_m}, \tag{13}$$

and

$$\alpha = \frac{2\phi_b}{\phi_c - \phi_b} \frac{r_c v_{w0}}{R_m} . \qquad (14)$$

Equation (12) represents the flux with respect to time, or flux decline due to cake layer growth. The transient cake layer thickness is thus described by

$$\delta_c = \left(\frac{\Delta P}{\mu r_c v_{w0}}\right) \left(\sqrt{1 + \alpha t} - 1\right). \qquad (15)$$

Pressure-dependent cake volume fraction, ϕ_c

In the initial stage of the dead-end membrane filtration, particle accumulation on the clean membrane surface is calculated with the initial permeate flux of Equation (13), which yields the highest hydrodynamic drag force on the particles stacked on the membrane surface. As filtration progresses, the hydrodynamic resistance grows with increasing cake thickness, and thus, hydrodynamic drag declines along with the flux. One might assume the cake volume fraction near the membrane surface must be higher than that at the cake–CP interface because it was formed under greater hydrodynamic drag forces. However, the hydrodynamic drag exerted on particles near the membrane surface is also reduced by declining flux. Particles will be reorganized by the local balance of hydrodynamic and interparticle forces, eliminating the porosity gradient. We assume this local reorganization is nearly instantaneous compared to the time scale of filtration, so that the (quasi) static equilibrium approximation remains valid. It is also assumed that the mean volume fraction across the cake layer does not significantly vary with time, and the porosity gradient vanishes when the cake thickness is several orders higher than the particle radius. Therefore, this study focuses on the structure of thick cake layers considering interparticle force in the regime of long-term, gradual flux decline, although simulation results show trends in the initial flux decline, not considered were the local hydrodynamic influence of the membrane surface on initial particle accumulation and the corresponding time-dependent evolution of cake structure. These effects may be significant for thin cake layers, but they are not significant for the thick cake layers considered here.

As mentioned earlier, a cake layer is defined as the region between the concentration polarization layer and the membrane surface, where the vertical porosity gradient is negligible. The scenario considered here is then analogous to a thermodynamic equilibrium state, in which a number of interacting particles are confined in a rectangular box of fixed volume. The box size is much larger than the particle size, and one of the box walls is freely movable. Particles inside the box interact according to a DLVO potential that depends on suspension properties such as particle size, solution ionic strength, and particle surface (zeta) potential. When the osmotic (or internal) pressure of interacting particles inside the box is balanced by the external pressure exerted against the movable wall, the box volume is constant, providing a specific structure for the particle configuration in the box. Similarly, the cake layer volume fraction in dead-end filtration is considered to be a function of applied pressure until the maximum packing fraction is achieved.

It is now worth comparing cake structures in dead-end and crossflow membrane filtration under identical physico-chemical and operating conditions. The axial flow along the membrane channel inside the cake layer is generally assumed to be negligible compared to the vertical permeate flow by accepting a no-slip boundary condition on the surface of the cake layer during crossflow filtration (Romero and Davis, 1988). Although shear flow probably does affect the cake structure during the initial stage of particle accumulation on the membrane surface, vertical flow will be dominant within a *thick* cake layer, so that the actual steady-state force balance is still primarily between vertical hydrodynamic drag and interparticle force. Past experimental investigations have shown that crossflow shear is relatively insignificant for microfiltration and ultrafiltration separations in which the cake layer is thin with respect to the channel height (Faibish *et al.*, 1998) because the cake layer does not significantly alter the tangential flow field (Davis, 1992). Therefore, the approach presented here may be valid for predicting the long-term gradual flux decline in crossflow membrane filtration when the long-term cake thickness is thin relative to the channel height.

SIMULATION

Interaction potential

The cake resistance alone governs flux decline in the dead-end membrane filtration model. Strong repulsive interactions between particles provide higher void fraction at a given applied pressure, so suspension properties are critical in determining the equilibrium cake structure and resultant flux decline. The model system is composed of charged, spherical particles interacting via a DLVO pair potential (Derjaguin and Landau, 1941; Verwey and Overbeek, 1948), which is comprised of attractive Lifshitz-van der Waals (VDW) and repulsive electrostatic double layer (EDL) interactions (Hunter, 1986).

The attractive VDW interactions between two colloidal particles originate from molecular interactions between permanent and/or induced dipoles in the particles. Pairwise summation of interparticle molecular interactions

was used to calculate overall particle–particle attraction (Hamaker, 1937). The interaction potential between two equal-sized colloids of radius a is

$$E_{VDW} = -\frac{A_H}{12}\left[\frac{4}{s^2} + \frac{4}{s^2-4} + 2\ln\left(1 - \frac{4}{s^2}\right)\right], \quad (16)$$

where A_H is the Hamaker constant, and $s(=r/a)$ is the dimensionless center-to-center distance. It may be noted that the VDW interaction energy diverges at contact ($s = 2$) so a cut-off separation distance, d_{min}, of 0.158 nm is used in Equation (16) (Hunter, 1986), and a hard-spherical repulsion is assumed at separation distances smaller than this value.

The linear superposition approximation (LSA) was used for EDL interactions under constant surface potential, with limitations of $\kappa r < 1$ and $\kappa a \geq 10$ (Bell et al., 1970). A matched asymptotic expansion was obtained with an error of order $1/(\kappa a)^2$ (Chew and Sen, 1982) for closer separations. Both expressions have a form of

$$E_{EDL} = Y\frac{128\pi n_0 a\gamma^2 k_B T}{\kappa^2}\frac{e^{-\kappa a(s-2)}}{s}, \quad (17)$$

where n_0 is the ion number concentration, k_B is the Boltzmann constant, and T is the absolute temperature. The quantity γ is defined by

$$\gamma = \tanh\left(\frac{ze\psi_s}{4k_B T}\right), \quad (18)$$

where z is the valence of ions in symmetrical z:z electrolyte, e is the electron charge, and ψ_s is the surface potential, which is replaced by the zeta potential ζ of particles (Bowen and Jenner, 1995) in this work. The Debye screening length, κ^{-1}, is given by

$$\kappa^{-1} = \sqrt{\frac{\varepsilon_0\varepsilon_r k_B T}{2e^2 z^2 n_0}} = \sqrt{\frac{\varepsilon_0\varepsilon_r k_B T}{2000e^2 N_A I}}, \quad (19)$$

where ε_0 is the permittivity of free space, ε_r is the dielectric permittivity of water, and N_A is the Avogadro's number. The pre-factor Y is given as

$$Y = \left(1 + \frac{\gamma^2}{2\kappa a}\right)^2 \quad (20)$$

in the work of Chew and Sen (1982).

Pressure components

In the past, hexagonal closed packing (HCP) was extensively used in theoretical research (Bacchin et al., 2002) for dead-end, as well as crossflow membrane filtration of colloidal suspensions. In these models, the cake layer osmotic pressure was determined by the sum of VDW, EDL, and entropic (ENT) contributions:

$$\Pi = \Pi_{ENT} + \Pi_{VDW} + \Pi_{EDL}. \quad (21)$$

The configurational entropic contribution was approximated by a hard sphere expression (Hall, 1972), and the result incorporated into a Wigner-Seitz cell approach (Bowen and Jenner, 1995) and the unifying model (Bacchin et al., 2002). This entropic expression, which reduces to the van't Hoff equation for small volume fractions, was obtained in an ordered state with specified volume fractions up to the maximum packing ratio for an HCP structure, 0.74. The van der Waals contribution was obtained by considering relaxation (Bowen and Jenner, 1995) of the Hamaker's expression (Hamaker, 1937), or by differentiating the van der Waals free energy of a hexagonal cell with respect to the number of solvent molecules in the cell (Jönsson and Jönsson, 1996). The electrostatic contribution to the osmotic pressure was calculated by solving Poisson-Boltzmann equation for the total ion concentration in a hexagonal cell (Bowen and Jenner, 1995; Jönsson and Jönsson, 1996). Bacchin et al. reorganized Bowen and Jenner's (1995) derivation of the electrostatic contribution, and used the expression for their unifying model (Bacchin et al., 2002).

All the theoretical studies for membrane filtration mentioned above, estimated the three components of the osmotic pressure *independently*, and added them together using the superposition principle. In other words, the three particulate systems were considered separately, and particles in each system were solely affected by hard sphere interactions, van der Waals attraction, or electrostatic double layer repulsion. The osmotic pressures of each system with only one kind of interparticle interaction were calculated *individually*, and summed to predict the osmotic pressure of a system where ENT, VDW and EDL interparticle interactions actually occur simultaneously.

In this study, the osmotic pressure Π due to interparticle interactions was determined from statistical mechanics and was related to the radial distribution function by

$$\Pi = nk_B T - \frac{2}{3}\pi n^2 a^3 \int_0^\infty s^3 g(s)\frac{dE}{ds}\,ds. \quad (22)$$

Here, n is the particle number concentration, $g(s)$ is the radial distribution function, and E is the total pair-interaction energy between two particles (Allen and Tildesley, 1994), which is given by

$$E = E_{VDW} + E_{EDL}. \quad (23)$$

In this work, short-range repulsion is represented by introducing a minimum cut-off distance d_{min} for estimating VDW interactions. Therefore, the divergence of van der Waals potential is prevented at the contact point,

$s = 2 + d_{min}/a$, denoted by σ^+, and Equation (22) is then rewritten as

$$\Pi = nk_BT + \frac{16}{3}\,\pi n^2 a^3 g(\sigma^+)k_BT$$

$$- \frac{2}{3}\,\pi n^2 a^3 \int_{\sigma^+}^{\infty} s^3 g(s)\,\frac{d}{ds}\,(E_{VDW} + E_{EDL})ds, \quad (24)$$

where the second term of the right-hand side is from the discontinuity of the radial distribution at $s = \sigma^+$ (Allen and Tildesley, 1994) due to the assumption of hard sphere interactions.

An analogy of Equation (21) in conjunction of Equation (24) provides

$$\Pi = \Pi_{ENT} + \Pi_{INT}, \quad (25)$$

where,

$$\Pi_{ENT} = nk_BT + \frac{16}{3}\,\pi n^2 a^3 g(\sigma^+)k_BT, \quad (26)$$

and,

$$\Pi_{INT} = \Pi_{VDW} + \Pi_{EDL}. \quad (27)$$

Here,

$$\Pi_{VDW} = -\frac{2}{3}\,\pi n^2 a^3 \int_{\sigma^+}^{\infty} s^3 g(s)\,\frac{dE_{VDW}}{ds}\,ds, \quad (28)$$

and,

$$\Pi_{EDL} = -\frac{2}{3}\,\pi n^2 a^3 \int_{\sigma^+}^{\infty} s^3 g(s)\,\frac{dE_{EDL}}{ds}\,ds. \quad (29)$$

The first term in Π_{ENT} of Equation (26) represents the van't Hoff expression that is valid in the dilute limit, and the second term indicates an additional entropic contribution, accounting for the deviation of entropic pressure from the dilute limit (Allen and Tildesley, 1994). The radial distribution functions in Figs. 2 and 3 represent the most and least repulsive scenarios considered in this work, respectively. The figures show that in the typical range of microfiltration operating pressures (i.e., up to about 100 kPa), particles undergo strong repulsion in the vicinity of other particles and cannot overcome the primary potential energy barrier. Under these repulsive conditions, the quantity $g(\sigma^+)$ is negligible, leaving the van't Hoff term as a major component of the entropic pressure. Equations (28) and (29) represent van der Waals attraction and electrostatic double layer repulsion, respectively.

When many-body interactions are not important, pairwise summation of a two-body potential provides a good approximation of total energy estimation for a given particulate system. Even if the pair-interaction is composed of several forces, use of the superposition principle does
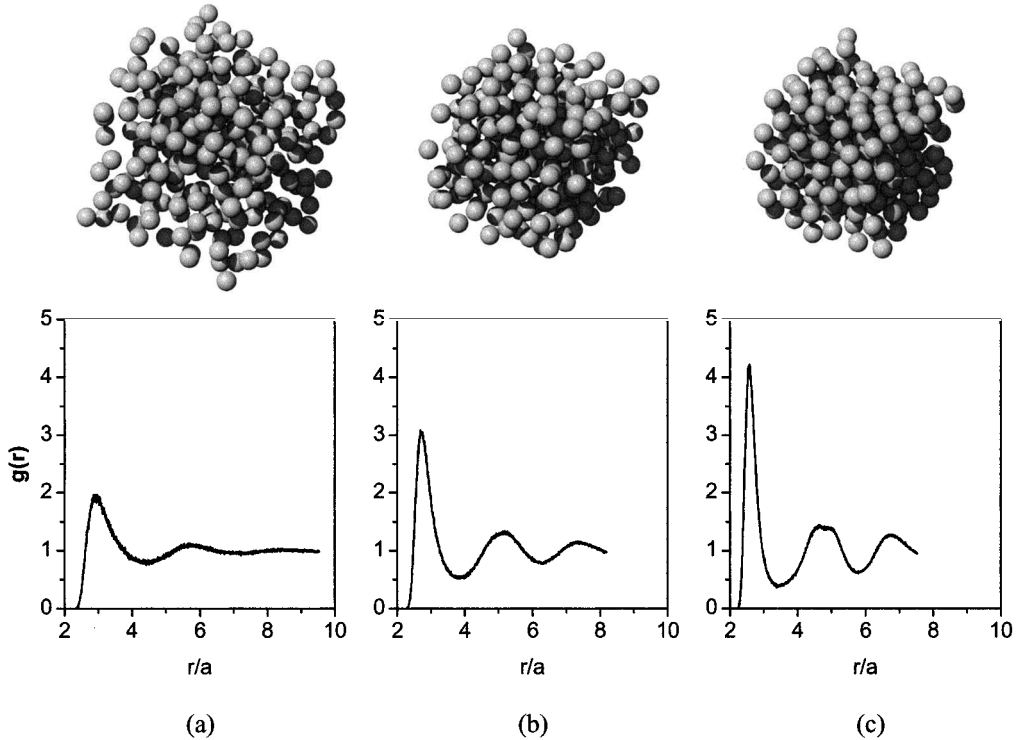
Figure 2. The cake structures and the corresponding radial distribution function $g(r)$ for applied pressure (a) 6.9 kPa (1.0 psi), (b) 34.5 kPa (5.0 psi), and (c) 103.4 kPa (15.0 psi). The physico-chemical condition employed are particle radius, 50 nm, zeta potential, -30 mV, and ionic strength, 10^{-3} M. The obtained volume fractions by the simulations are (a) 0.147, (b) 0.237, and (c) 0.308.
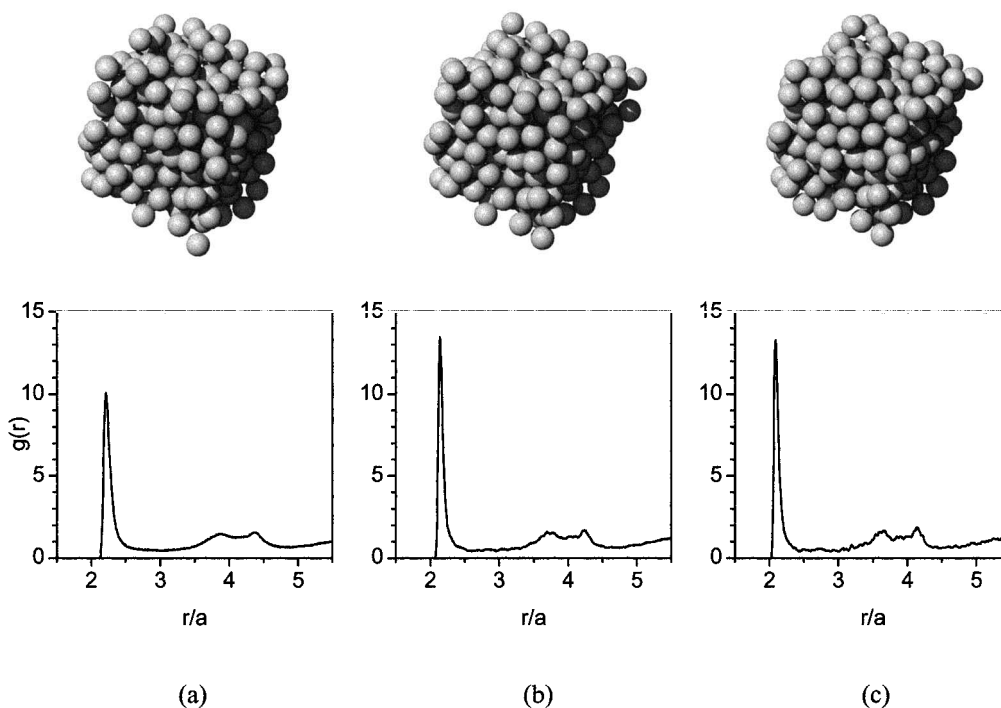
Figure 3. The cake structures and the corresponding radial distribution function $g(r)$ for applied pressure (a) 6.9 kPa (1.0 psi), (b) 34.5 kPa (5.0 psi), and (c) 103.4 kPa (15.0 psi). The physico-chemical condition employed are particle radius, 200 nm, zeta potential, -30 mV, and ionic strength, 10^{-2} M. The obtained volume fractions by the simulations are (a) 0.473, (b) 0.530, and (c) 0.571.

not fail because the ensemble of particle configuration is established based on total forces acting on each particle due to the rest of the other particles. However, averaging the radial distribution functions of systems with different interparticle interactions is not identical to calculating the function accounting for the total interparticle interactions simultaneously acting on each particle. This is already verified by investigating the contact value of the radial distribution functions at $s = \sigma^+$ in Figs. 2 and 3. As described in Equation (23), the DLVO interaction is a superposition of the van der Waals attraction and the electrostatic double layer repulsion. If the resulting pairwise interaction is repulsive, the additional entropic contribution of the osmotic pressure is suppressed because hard-sphere collisions are prevented by the potential energy barrier. Consequently, the addition of an independently calculated hard-sphere entropic contribution to the osmotic pressure may not be justified.

In this study, the particle configuration was assumed to be homogeneous and isotropic (but not crystallized) with a given configurational structure. This structure is characterized by the radial distribution function, which is solely determined by the total interparticle interactions and the applied pressure during the Monte Carlo simulation. It is therefore unnecessary to assume *a priori* any

specific structure of the cake layer. Furthermore, the osmotic pressure is more accurately estimated than in previous studies by considering the superposition of interacting forces, not the osmotic pressures determined individually.

Isothermal-isobaric Monte Carlo simulation

The equilibrium structure of a cake composed of $N(=256)$ particles interacting according to the pair interactions described in Equations (16) and (17) with (20) was determined by isothermal-isobaric (or called NPT) Monte Carlo simulations (Allen and Tildesley, 1994). One simulation cycle consisted of the standard Metropolis Monte Carlo (MMC) (Metropolis *et al.*, 1953) simulation and a configurational scaling component. The initial particle configuration was a randomly distributed structure of volume fraction less than 0.1 with no particles overlapping. Overlap was defined as the center-to-center distance between any two particles less than $2a + d_{min}$.

In each step of one MMC cycle, the configuration was updated by randomly moving each particle and determining the energy change based on that move. A move was accepted or rejected according to the transition probability

$$P_{\text{MMC}} = \begin{cases} 1 & \text{if } E_{\text{conf}}^{\text{new}} - E_{\text{conf}}^{\text{old}} \leq 0, \\ \exp(-\beta(E_{\text{conf}}^{\text{new}} - E_{\text{conf}}^{\text{old}})) & \text{otherwise} \end{cases} \quad (30)$$

where $E_{\text{conf}}^{\text{new}}$ and $E_{\text{conf}}^{\text{old}}$ were the total interaction energies due to the new and old particle configurations, respectively, and $\beta = 1/k_B T$. One MMC cycle consisted of $N(=256)$ steps, which were associated with the move of all the particles in a sequential order. Periodic boundary conditions were implemented to reflect (approximately) homogeneous cake structure in a simulation box of fixed volume. The actual cake buildup is based on continuous particle-accumulation on the cake surface, caused by solvent flow. To describe this interfacial phenomenon and investigate such hydrodynamic effects, more rigorous simulation approaches [i.e., hydrodynamic force-bias Monte Carlo (Kim *et al.*, 2001) or Stokesian dynamics (Bossis *et al.*, 1991)] should be applied. However, the interest here is in determining homogeneous particle-configurations within a cake layer formed by means of a force balance. The focus is not on the interface between the CP and cake layers or even the membrane surface, but in the bulk-phase of the cake during long-term, gradual flux decline. Therefore, biased trial movement of particles using periodic boundary conditions (even in a direction of the permeate flow) would not affect the particle configurations significantly.

In the configurational scaling component, a new state was generated by a random volume change from V^{old} to $V^{\text{new}} (= V^{\text{old}} + \Delta V)$ and the corresponding particle configuration scaled by $\sqrt{V^{\text{new}}/V^{\text{old}}}$, keeping the structure unchanged. A volume change (VC) was accepted or rejected by the transition probability

$$p_{\text{vc}} = \begin{cases} 1 & \text{if } \Delta h \leq 0, \\ \exp(-\beta \Delta h) & \text{otherwise} \end{cases}, \quad (31)$$

where Δh was a quantity closely related to the enthalpy change, defined by

$$\Delta h = \Delta E_{\text{conf}}^{\text{scale}} + \Delta P \, (V^{\text{new}} - V^{\text{old}}) \\ - \beta^{-1} \, N \ln \, (V^{\text{new}}/V^{\text{old}}). \quad (32)$$

In Equation (32), $\Delta E_{\text{conf}}^{\text{scale}}$ is the energy change caused by configurational scaling, not the individual particle move, N is the number of particles, and ΔP is the applied (or external) pressure. The applied pressure governs cake structure in following ways while the system is on a way to an equilibrium state. If the random volume change ΔV, of which the maximum value was being adjusted for faster convergence to an equilibrium state during simulation, is positive, then the configurational energy change $\Delta E_{\text{conf}}^{\text{scale}}$ becomes negative due to the scaling of the particle coordinates, and vice versa. Without considering the third term of Equation (32), which stems from normal-

ization of p_{vc}, $\Delta E_{\text{conf}}^{\text{scale}}$ and $\Delta P \Delta V$ are always competing with each other because of their different signs. At high applied pressure and properly adjusted ΔV, the effect of the configurational energy change is smaller than that of $\Delta P \Delta V$. If $\Delta V > 0$, the positive value of $\Delta P \Delta V$ causes less transition probability of the system from small volume to large volume. In the opposite case ($\Delta V < 0$), high pressure forces the system to reduce the volume until it reach a certain equilibrium state, in which the configuration energy change is comparable to applied pressure multiplied by the volume change. Therefore, a certain cake structure is generated at given applied pressure by the transition probabilities, and thus, the higher the pressure, the lower the cake porosity.

High-performance parallel computation

Parallel computation using Message Passing Interface (MPI) (Gropp *et al.*, 1997) was used for high-performance computing in a Beowulf Linux cluster (Sterling, 2001; Vazhkudai *et al.*, 2002) composed of 16 PCs. Each computer has 1.9 GHz Intel Pentium IV CPU and 1-GB random access memory. They are connected to a data switch (NETGEAR Inc., Santa Clara, CA) through 100 Mega-Bits Per Second (MBPS) network adaptors imbedded in motherboards. User home directories are exported from a Network File System (NFS) server to the rest of 15 nodes, and commonly used for file sharing and execution of the parallel FORTRAN program. All the computations were performed using a Master-Slave algorithm (Gropp *et al.*, 1997), with communication through MPI using a remote shell (rsh).

When an NPT-MC simulation run begins, the master node reads a particle configuration composed of 256 particles, and sends the particle position data to the other 15 slave nodes using a subroutine called MPI_BCAST (Gropp *et al.*, 1997). After receiving the particle coordinates, each slave node performs its own NPT-MC simulation with different seeds for the random number generator. Therefore, during the simulation each node has its own particle configuration, but it equally has 256 particles with an identical two-body interaction potential. After every 20 cycles of the simulation, the master node collects all statistical data from all nodes. One NPT-MC simulation is performed with 4,800 cycles, which is equivalent to 1,228,800 MC steps in the standard MMC simulation using the canonical ensemble.

The cake structure for a given set of physico-chemical conditions (i.e., particle radius, ionic strength, zeta potential, and Hamaker constant) was first determined at the lowest applied pressure, 6.9-kPa (1-psi), assuming a very sparse initial particle configuration with porosity greater than 0.9. The corresponding equilibrium structure was obtained within 1,000 MC cycles, and this state was

verified by watching the system energy variance along with MC cycles, and by comparing the applied pressure and the returned osmotic pressure (discussed below). One equilibrium structure generated at each pressure was used as the initial structure for the next pressure. Applied pressure was increased in 6.9-kPa (1-psi) increments, and 480 cycles was sufficient for the system to reach equilibrium at each new pressure. In most cases, each run at a given applied pressure took about 5 to 6 minutes for 480 cycles of equilibration and 4,800 cycles of statistical sampling.

RESULTS AND DISCUSSION

Isothermal-isobaric Monte Carlo simulations using the DLVO interaction potential described above were performed for various operating conditions and physico-chemical suspension properties. The parameters used in the simulations are listed in Table 1.

Cake layer structure

When applied pressure increases, the cake layer becomes less porous, and the corresponding radial distribution function resembles a more solid-like structure. This behavior is demonstrated in Figs. 2 and 3, and some interesting points are clarified. The distribution functions were obtained by ensemble averages of $3,840(=240 \times 16)$ particle configurations sampled in every 20 MC cycles during the total 4,800 cycles at a given applied pressure. The corresponding cake structure is the snapshot of the configuration, taken at the end of the equilibrium simulation by the master node of the Beowulf Linux cluster composed of 16 computers.

Figure 2 presents equilibrium cake structure and radial distribution function for a 50-nm particle with surface zeta potential of -30 mV at simulated ionic strength of

10^{-3} M. The specific data in Fig. 2a, b, and c illustrate the influence of applied pressure on equilibrium cake structure. In particular, Fig. 2a presents a snapshot at the lowest pressure, 6.9 kPa (1 psi). The resulting cake layer has a disordered and sparse particle configuration, and this is verified by the radial distribution function. A $g(r)$ with low and smooth peaks suggests a dilute, disordered particle suspension. The structure shown in Fig. 2(b) illustrates an intermediate stage between the low and high applied pressures. At the highest pressure of 103.4 kPa (15 psi) shown in Fig. 2c, the configuration is more compact and ordered compared with those of Fig. 2a and 2b. This is verified by the corresponding radial distribution function having relatively high second and third peaks. The data illustrated in Fig. 2c represent highly repulsive physico-chemical suspension properties due to the small particle size ($a = 50$ nm) and low ionic strength ($I = 10^{-3}$ M). The repulsive conditions create a more ordered equilibrium state even though the particle volume fraction is still relatively low ($\phi_c = 0.308$), implying that ordering could take place before a maximum volume fraction is reached.

Figure 3 shows equilibrium cake configurations for a larger particle ($a = 200$ nm) at a higher ionic strength ($I = 10^{-2}$ M), and at the applied pressures of (a) 6.9, (b) 34.5, and (c) 104.3 kPa (1, 5, and 10 psi, respectively). These physico-chemical suspension properties represent the least repulsive system analyzed in this work based on the parameters listed in Table 1. The high peaks in the radial distribution function are due to long-range DLVO interactions, in which van der Waals attraction is significant at large separations. As applied pressure increases, the second and third peaks become narrower and sharper, representing a transition from a randomly agglomerated state to a more ordered state. Careful investigation of Fig. 3b and 3c shows that the height of the first peak of the radial distribution function with an applied pressure of

Table 1. Parameters used for prediction of the cake structure.

Bulk volume fraction, ϕ_b (−)	0.0001
Particle radius, a (nm)	50, 100, 200
Hamaker constant, A_H (J)[a]	4.6×10^{-21}
Zeta potential, ζ (mV)	$-30, -40, -50$, and -90
Ionic strength, IS (M)	$10^{-2}, 10^{-3}$, and 10^{-4}
Valence of ions, z (−)	1
Minimum cutoff distance, d_{min} (nm)	0.158
Solvent dielectric permittivity, ε_r (−)	78.54
Pressure, ΔP (kPa)	6.9–103.4 (1–15 psi)
Temperature, T (K)	298.5

[a]Silica particle is chosen as a model colloid in this work. The recently reported Hamaker constant of silica particle (Bergström, 1997) is employed to perform MC simulations.
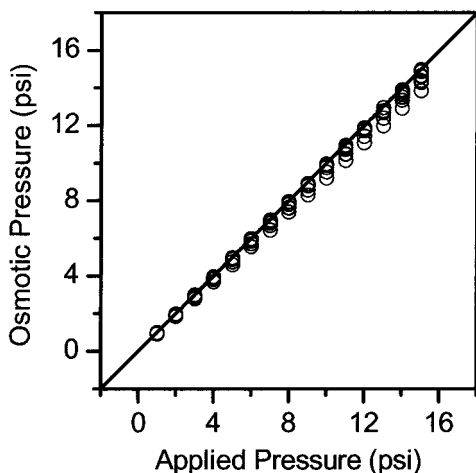
Figure 4. Applied pressures vs. returned osmotic pressures calculated by the corresponding radial distribution functions.

34.5 kPa (5 psi) is higher than that with pressure of 103.4 kPa (15 psi). The peak of Fig. 3c, however, is closer to the contact point, indicating a denser structure and higher osmotic pressure calculated from Equation (24).

Figure 12 of Bowen and Jenner's work (Bowen and Jenner, 1995) presents contradictory results. In most cases except for moderately low zeta potential (10 mV), the electrostatic contribution to the, "disjoining pressure" (termed osmotic pressure here) is predominant over the other components. Note that the Hamaker constant, the ionic strength, and zeta potential used in Fig. 12c of their work and Fig. 3 of the present article is in a same order while the particle size of BSA (Bovine Serum Albumin), ca. 3 nm, is two orders less than that of the silica particle, 200 nm. Obviously, the resulting force exerted on larger particles is less repulsive due to the larger volume of particles and faster decay of electrostatic potential of Equation (17). In this case, the entropic contribution in their work becomes more significant compared to the others. However, Fig. 3 of this study clearly indicates that the entropic contribution to the osmotic pressure is negligible due to the vanishing contact value of the radial distribution functions, even if a much larger particle (200 nm) was used. Although the superposition of pressure components is arguably valid to rigorously estimate the osmotic pressure of interacting colloidal particles, the importance of this analysis is that superimposition of the entropic component may result in significant overestimation of the osmotic pressure, corresponding with an overestimate of permeate flux.

Cake layer osmotic pressure

To verify the accuracy of NPT Monte Carlo simulations, Fig. 4 compares the applied and returned osmotic

pressures for all physico-chemical conditions simulated. At low applied pressure, the corresponding osmotic pressure is almost identical to the applied pressure, and at high applied pressure, the returning osmotic pressure is slightly less than applied pressure. This difference is within 5% of its maximum, indicating the accuracy of the simulations performed in this study. The primary reason for the difference is shown in Equation (24). It comes from the sensitive integration of the radial distribution function multiplied by the derivative of the total interaction energy. Both of these functions are rapidly varying with respect to the center-to-center distance, r, especially near the contact region for which the integration contribution is most dominant.
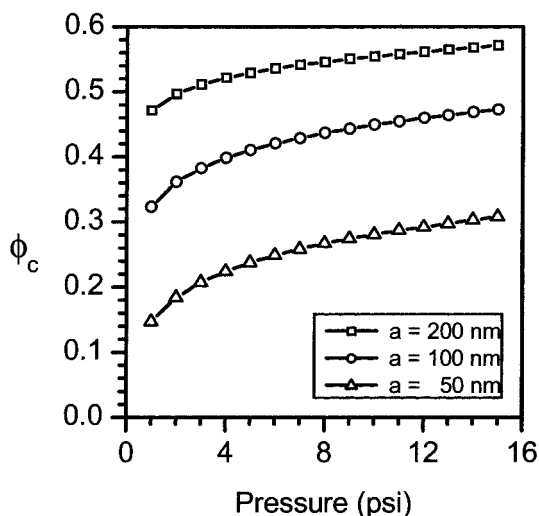
Cake layer volume fractions

Figures 5, 6, and 7 illustrate the influence of particle zeta potential, particle size, and bulk solution ionic strength on cake layer volume fraction, respectively. The data of Fig. 5 show that a greater zeta potential (in magnitude) yields a lower cake volume fraction due to more EDL repulsion. However, the differences in the cake volume fraction with a given applied pressure in Fig. 5 are subtle. The zeta potential is embedded in a tangent hyperbolic function in Equation (18), so as zeta potential increases monotonously the quantity γ reaches an asymptotic value of unity above ± 25 mV for a 1:1 electrolyte. Therefore, changes in zeta potential provide a relatively subtle difference in the electrostatic double layer repulsion, and thus, the cake structure.

Figure 6 shows that as particle size increases with all
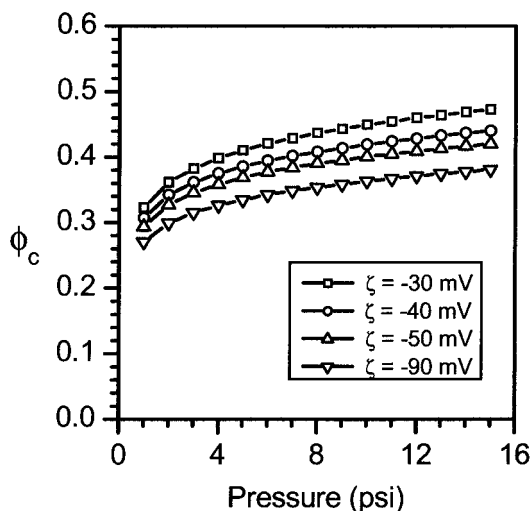
Figure 5. Effect of zeta potential on the cake volume fraction. The physico-chemical conditions employed were particle size, 100 nm, and ionic strength, 10^{-3} M.

Figure 6. Effect of particle size on the cake volume fraction. The physico-chemical conditions employed were ionic strength, 10^{-3} M, and zeta potential, -30 mV.

other physico-chemical conditions held constant, the cake layer volume fraction increases. It is well known that for larger particles the relative influence of van der Waals attraction is enhanced and electrostatic double layer repulsion is suppressed. The data presented in Fig. 7 reveals that increasing the ionic strength results in a higher cake volume fraction. High ionic strength reduces the effective range of electrostatic repulsion by shortening the Debye screening length, κ^{-1}. Inversely, elongating κ by increasing ionic strength contributes to a faster decay of the interaction potential with respect to s. In a less repulsive suspension (represented by larger colloids and/or higher ionic strength in Figs. 6 and 7, respectively) the cake volume fraction increases rapidly at low pressures and approaches an asymptotic limit at higher pressures. In the case of small particles and low ionic strength, the cake volume fraction increases monotonously over the entire pressure range because strong repulsion leads to a more porous cake structure and excluded volume effects are less important.

Permeate flux decline

Figure 8 shows that the initial flux decline is more severe as particle size decreases. Although cake layers composed of smaller particles exhibited higher porosity in Fig. 6, the net effect of interparticle interactions is less important than that of particle size. The cake layer composed of smaller particles offers more hydraulic resistance to permeation because the specific cake resistance depends inversely on the square of the particle size, as shown in Equation (9). This explains the rapid initial flux

decline, which has also been observed experimentally (Hong *et al.*, 1997).

A secondary influence of particle size may be that smaller particles possess fewer permanent or induced dipole moments, which are the origin of the van der Waals attraction. Thus, the role of the electrostatic double layer interaction is relatively more important as particle size decreases. Smaller particles undergo higher repulsion due to this relatively enhanced electrostatic double layer interaction, resulting in a more porous cake layer.

Figure 9 shows that the permeate flux decline becomes more rapid as ionic strength increases. The effective scale of the electrostatic double layer interaction, the Debye screening length, is reduced at higher ionic strengths. Similar trends have been observed in other theoretical and experimental research (Mcdonogh *et al.*, 1984, 1989; Bowen and Jenner, 1995; Zhu and Elimelech, 1997).

In experiments, it is difficult to independently control zeta potential of particles, but Fig. 10 illustrates what the sole effect of varied zeta potential would be on flux decline. As shown in Fig. 5, this effect is less significant compared to that of particle size or ionic strength, but the trend indicates that higher zeta potential enhances the permeate flux by maintaining a more porous cake layer. Similar trends to those displayed in Figs. 8 and 9 were recently reported (Faibish *et al.*, 1998), although the experiments were based on crossflow membrane filtration.

Application to crossflow membrane filtration

The approach used here is safely restricted to certain conditions: (1) cake resistance is dominant compared to
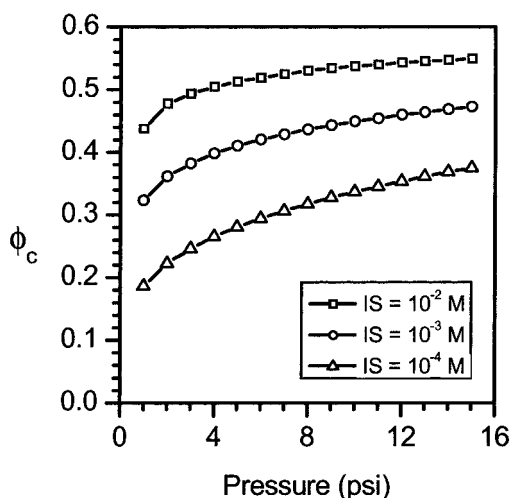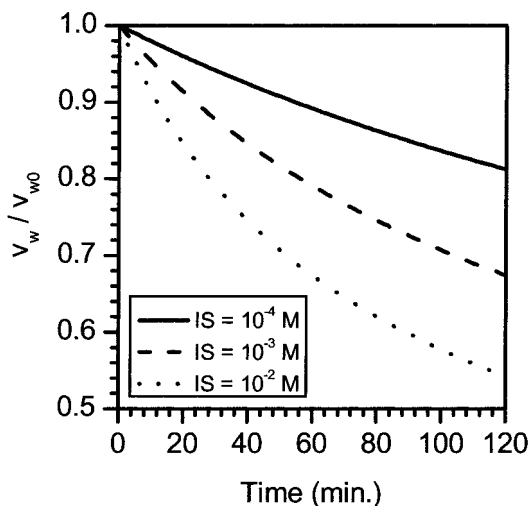

Figure 7. Effect of ionic strength on the cake volume fraction. The physico-chemical conditions employed were particle size, 100 nm, and zeta potential, -30 mV.
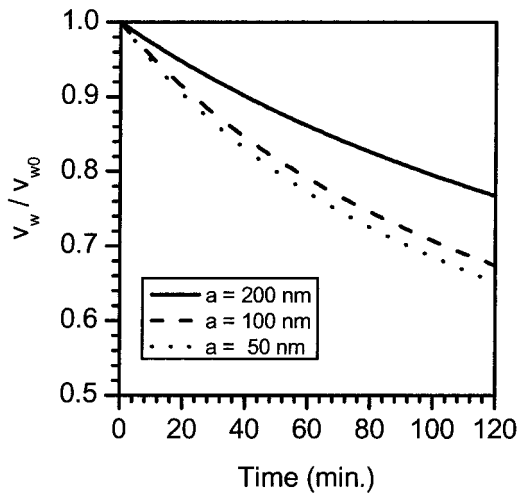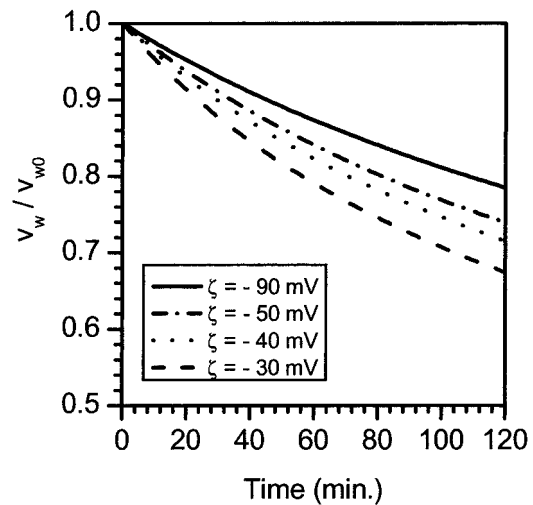
Figure 8. Effect of particle size on the permeate flux decline. The physico-chemical conditions employed were pressure, 69.0 kPa (10 psi), membrane resistance, 10^{12} m^{-1}, ionic strength, 10^{-3} M, and zeta potential, -30 mV. The cake volume fraction for particle size, 50, 100, and 200 nm are 0.281, 0.449, and 0.554, respectively.

membrane and CP resistance, (2) cake layer thickness is several orders larger than particle radius, (3) cake structure is approximately homogeneous across the cake layer, and (4) total interparticle force is repulsive and balanced solely by the transverse hydrodynamic drag.

For noninteracting hard spheres, or even attractive par-

Figure 9. Effect of ionic strength on the permeate flux decline. The physico-chemical conditions employed were pressure, 69.0 kPa (10 psi), membrane resistance, 10^{12} m^{-1}, particle size, 100 nm, and zeta potential, -30 mV. The cake volume fraction for ionic strength, 10^{-4}, 10^{-3}, and 10^{-2} M are 0.337, 0.449, and 0.538, respectively.

Figure 10. Effect of zeta potential on the permeate flux decline. The physico-chemical conditions employed were pressure, 69.0 kPa (10 psi), membrane resistance, 10^{12} m^{-1}, particle size, 100 nm, and ionic strength, 10^{-3} M. The cake volume fraction for zeta potential, -30, -40, -50, and -90 mV are 0.449, 0.419, 0.401, and 0.367, respectively.

ticles, the no-slip boundary condition on axial flow at the membrane or cake surface implicitly supports the availability of our approach for predicting permeate flux during the crossflow membrane filtration (Song and Elimelech, 1995). However, repulsive particles produce more porous cake structures, which may allow some axial flow penetrate into the cake layer. The hydrodynamic forces exerted by particles will be different in magnitude and direction near the boundary of the CP and cake layers. The phenomenon would be obvious for thin cake layers, where cake resistance may not predominate over membrane resistance, so a detailed dynamic simulation must be performed to more accurately predict permeate flux. Comparison of experimental results with simulations for thin cake layers in crossflow conditions would provide valuable insight into a poorly understood system, but is beyond the scope of this investigation.

CONCLUDING REMARKS

A fundamental statistical mechanics approach for predicting the influence of interparticle interactions on flux decline during dead-end membrane filtration of charged colloidal particles was presented. The approach presented here provides a direct link between the interparticle interactions and flux decline behavior using a fundamental and rigorous method of statistical mechanics by predicting the cake structure and corresponding volume fraction with given physico-chemical suspension and operating

conditions. These conditions include the particle Hamaker constant, size, and zeta potential, solution ionic strength, and applied pressure. The approach predicted the cake structure from NPT Monte Carlo simulations utilizing the superposition principle for calculation of pair-wise interaction potential, and characterized the cake layer with an average porosity and radial distribution function. The significance of the approach was that realistic cake structures were predicted by rigorously accounting for physico-chemical suspension properties and operating conditions.

The pressure-dependent cake volume fractions were then incorporated into the Kozeny-Carman equation, which led to predictions of permeate flux decline when coupled with a dead-end cake filtration model. The pressure-dependent cake volume fraction was found to be highly dependent on initial flux, particle size, and bulk solution ionic strength, and weakly dependent on particle surface (zeta) potential. These findings are in absolute agreement with previously published experimental data of Hong *et al*. (1997) and Faibish *et al.* (1998). Therefore, it is concluded that the simulation method presented here provided good quantitative predictions of cake porosity, as well as permeate flux under operating conditions relevant to practical microfiltration separations. Finally, this work suggests that for the first time, *a priori* prediction of filtration performance for monodisperse suspensions can be made without assuming a cake structure and, hopefully, one can now predict the long-term gradual flux decline in dead-end membrane filtration more accurately.

REFERENCES

ALLEN, M.P., and TILDESLEY, D.J. (1994). *Computer Simulation of Liquids*. Oxford, UK, Clarendon Press.

BACCHIN, P., SI-HASSEN, D., STAROV, V., CLIFTON, M.J., and AIMAR, P. (2002). A unifying model for concentration polarization, gel-layer formation and particle deposition in cross-flow membrane filtration of colloidal suspensions. *Chem. Eng. Sci.* **57,** 77.

BATCHELOR, G.K. (1972). Sedimentation in a dilute dispersion of spheres. *J. Fluid Mech.* **52,** 245.

BELL, G.M., LEVINE, S., and MCCARTNEY, L.N. (1970). Approximate methods of determining the double-layer free energy of interaction between two charged colloidal spheres. *J. Colloid Interface Sci.* **33,** 335.

BERGSTRÖM, L. (1997). Hamaker constants of inorganic materials. Adv. Colloid Interface Sci. **70,** 125.

BHATTACHARJEE, S., KIM, A.S., and ELIMELECH, M. (1999). Concentration polarization of interacting solute particles in cross-flow membrane filtration. *J. Colloid Interface Sci.* **212,** 81.

BHATTACHARJEE, S., SHARMA, A., and BHATTACHARYA, P.K. (1994). Surface interactions in osmotic pressure controlled flux decline during ultrafiltration. *Langmuir* **10,** 4710.

BOSSIS, G., MEUNIER, A., and SHERWOOD, J.D. (1991). Stokesian dynamics simulations of particle trajectories near a plane. Physics of Fluids A-Fluid Dynamics **3,** 1853.

BOWEN, W.R., and JENNER, F. (1995). Dynamic ultrafiltration model for charged colloidal dispersions—a wigner-seitz cell approach. *Chem. Eng. Sci.* **50,** 1707.

CARMAN P.C. (1939). Permeability of saturated sands soils and clays. *J. Agric. Sci.* **29,** 262.

CHEW, W.C., and SEN, P.N. (1982). Potential of a sphere in anionic solution in thin double-layer approximations. *J. Chem. Phys.* **77,** 2042.

DAVIS, R.H. (1992). Modeling of fouling of crossflow microfiltration membranes. *Sep. Purif. Methods* **21,** 75.

DECAROLIS, J., HONG, S., and TAYLOR, J. (2001). Fouling behavior of a pilot scale inside-out hollow fiber uf membrane during dead-end filtration of tertiary wastewater. *J. Membr. Sci.* **191,** 165.

DERJAGUIN, B.V., and LANDAU, L.D. (1941). Theory of the stability of strongly charged lyophobic sols and of the adhesion of strongly charged particles in solutions of electrolytes. *Acta Physicochim. URSS* **14,** 733.

ELIMELECH, M., and BHATTACHARJEE, S. (1998). A novel approach for modeling concentration polarization in crossflow membrane filtration based on the equivalence of osmotic pressure model and filtration theory. *J. Membr. Sci.* **145,** 223.

ELIMELECH, M., GREGORY, J., JIA, X., and WILLIAMS, W. (1995). *Particle Deposition and Aggregation: Measurement, Modeling, and Simulation*. Oxford: Butterworth Heinemann.

FAIBISH, R.S., ELIMELECH, M., and COHEN, Y. (1998). Effect of interparticle electrostatic double layer interactions on permeate flux decline in crossflow membrane filtration of colloidal particles: An experimental investigation. *J. Colloid Interface Sci.* **204,** 77.

GROPP, W., LUSK, E., and SKJELUM, A. (1997). *Using MPI: Portable Parallel Programming with the Message-Passing Interface*. Cambridge, MA, The MIT Press.

HALL, K.R. (1972). Another hard sphere equation of state. *J. Chem. Phys.* **57,** 2252.

HAMAKER, H.C. (1937). The London-van der Waals attraction between spherical particles. *Physica* **4,** 1058.

HAPPEL, J. (1958). Viscous flow in multiparticle systems: Slow motion of fluids relative to beds of spherical particles. *AIChE J.* **4,** 197.

HAPPEL, J., and BRENNER, H. (1991). *Low Reynolds Number Hydrodynamics.* Dordrecht, Kluwer.

HOLT, W.J.C., CARNIE, S.L., and CHAN, D.Y.C. (1995). Colloidal interactions in low volume fraction pressurized ultrafiltration systems. *J. Colloid Interface Sci.* **173,** 304.

HONG, S., FAIBISH, R.S., and ELIMELECH, M. (1997). Kinetics of permeate flux decline in crossflow membrane filtration of colloidal suspensions. *J. Colloid Interface Sci.* **196,** 267.

HUNTER, R.J. (1986). *Foundations of Colloid Science.* New York: Oxford Univ. Press.

JÖNSSON, A.S., and JÖNSSON, B. (1996). Ultrafiltration of colloidal dispersions—A theoretical model of the concentration polarization phenomena. *J. Colloid Interface Sci.* **180,** 504.

KEDEM, O., and KATCHALSKY, A. (1958). Thermodynamic analysis of the permeability of biological membranes to non-electrolytes. *Biochim. Biophys. Acta* **37**, 229.

KIM, A.S., BHATTACHARJEE, S., and ELIMELECH, M. (2001). Shear-induced reorganization of deformable molecular assemblages: Monte Carlo studies. Langmuir **17,** 552.

MCDONOGH, R.M., FANE, A.G., and FELL, C.J.D. (1989). Charge effects in the cross-flow filtration of colloids and particulates. *J. Membr. Sci.* **43,** 69.

MCDONOGH, R.M., FELL, C.J.D., and FANE, A.G. (1984). Surface charge and permeability in the ultrafiltration of non-flocculating colloids. *J. Membr. Sci.* **21,** 285.

METROPOLIS, N., ROSENBLUTH, A.W., ROSENBLUTH, M.N., TELLER, A.H., and TELLER, E. (1953). Equation of state calculations by fast computing machines. *J. Chem. Phys.* **21,** 1087.

PETSEV, D.N., STAROV, V.M., and IVANOV, I.B. (1993). Concentrated dispersions of charged colloidal particles—Sedimentation, ultrafiltration and diffusion. *Colloid Surf. A* **81,** 65.

REIHANIAN, H., ROBERTSON, C.R., and MICHAELS, A.S. (1983). Mechanisms of polarization and fouling of ultrafiltration membranes by proteins. *J. Membr. Sci.* **16,** 237.

REITH, C., and BIRKENHEAD, B. (1998). Membranes enabling the affordable and cost effective reuse of wastewater as an alternative water source. *Desalination* **117,** 203.

ROMERO, C.A., and DAVIS, R.H. (1988). Global model of crossflow microfiltration based on hydrodynamic particle diffusion. *J. Membr. Sci.* **39,** 157.

ROMERO, C.A., and DAVIS, R.H. (1990). Transient model of crossflow microfiltration. *J. Membr. Sci.* **45,** 13.

SONG, L.F., and ELIMELECH, M. (1995). Theory of concentration polarization in crossflow filtration. *J. Chem. Soc. Faraday Trans.* **91,** 3389.

STERLING, T.L. (2001). *Beowulf Cluster Computing with Linux.* Cambridge, MA: MIT Press.

VAN DEN BERG, G.B., and SMOLDERS, C.A. (1990). Flux decline in ultrafiltration processes. *Desalination* **77,** 101.

VAZHKUDAI, S., SYED, J., and MAGINNIS, T. (2002). PODOS—The design and implementation of a performance oriented Linux cluster. *Future Gen. Comp. Sys.* **18,** 335.

VERWEY, E.J., and OVERBEEK, J.T.G. (1948). *Theory of the Stability of Lyophobic Colloids.* Amsterdam: Elsevier.

VILKER, V.L., COLTON, C.K., and SMITH, K.A. (1981). The osmotic pressure of concentrated protein solutions: Affect of concentration and pH in saline solutions of bovine serum albumin. *J. Colloid Interface Sci.* **79,** 548.

WIESNER, M.R., HACKEY, J., SANDEEP, S., JACANGELO, J.G., and LAINE, J.M. (1994). Cost estimates for membrane filtration and conventional treatment. *J. Am. Water Work Assoc.* **86,** 33.

WILLEMSE, R.J.N., and BREKVOORT, Y. (1999). Full-scale recycling of backwash water from sand filters using dead-end membrane filtration. *Water Res.* **33,** 3379.

ZEMAN, L.J., and ZYDNEY, A.L. (1996). *Microfiltration and Ultrafiltration: Principles and Applications.* New York: Marcel Dekker.

ZHU, X.H., and ELIMELECH, M. (1997). Colloidal fouling of reverse osmosis membranes: Measurements and fouling mechanisms. *Environ. Sci. Technol.* **31**, 3654.